Nanoscale

PAPER

View Article Online
View Journal | View Issue

Cite this: *Nanoscale*, 2024, **16**, 10318

An insight, at the atomic level, into the structure and catalytic properties of the isomers of the Cu_{22} cluster†

Huimin Zhou,‡[a] Tao Yang,‡[a] Huijuan Deng,‡[a] Yapei Yun,[a] Shan Jin, *[a] Lin Xiong*[b] and Manzhou Zhu *[a]

Received 7th March 2024,
Accepted 28th April 2024

DOI: 10.1039/d4nr00973h

rsc.li/nanoscale

The study of structural isomerism in copper nanoclusters has been relatively limited compared to that in gold and silver nanoclusters. In this work, we present the controlled synthesis and structures of two isomeric copper nanoclusters, denoted as **Cu_{22}-1** and **Cu_{22}-2**, whose compositions were determined to be $Cu_{22}(SePh)_{10}(Se)_6(P(Ph\text{-}^4F)_3)_8$ through single-crystal X-ray diffraction (SCXRD). The structural isomerism of **Cu_{22}-1** and **Cu_{22}-2** arises from the different arrangements of a few Cu(SeR)(PR_3) motifs on the surface structure. These subtle changes in the surface structure also influence the distortion of the core and the spatial arrangement of the clusters, and affect the electronic structure. Furthermore, due to their distinct structures, **Cu_{22}-1** and **Cu_{22}-2** exhibit different catalytic properties in the copper-catalyzed [3 + 2] azide–alkyne cycloaddition (CuAAC). Notably, **Cu_{22}-1** demonstrates efficient catalytic activity for photoinduced AAC, achieving a yield of 90% within 1 hour. This research contributes to the understanding of structural isomerism in copper nanoclusters and offers insights into the structure–function relationship in these systems.

Introduction

Ligand-protected nanoclusters have attracted significant attention due to their promising applications in catalysis, optical waveguides, fluorescence, and more.[1–9] The increasing number of structurally-determined clusters has led to the discovery of various types of nanocluster isomerism, including chiral isomerism and structural isomerism, which serve as valuable models for investigating structure–property relationships.[10–17] Chiral isomerism is often observed in the crystal lattice, while structural isomerism can be achieved through ligand engineering or controlled synthesis methods. However, compared to chiral isomerism, the existence of "literal" nanocluster structural isomers, composed of identical constituent metals and ligands, is rarely reported. To date, only seven pairs of such isomers have been fully structurally determined, namely Au_4Cu_4,[18] Au_9,[19] Au_{23},[10] Au_{28},[20] Au_{36},[21] Au_{38},[22] and Au_{42}.[23] The discovery of structural isomerism has greatly contributed to our understanding of the correlation between cluster structures and their properties. For instance, the $Au_{36}(SR)_{24}$ cluster, with a two-dimensional (2D) arrangement of Au_4 tetrahedral units, has been found to exhibit higher efficiency in the intramolecular hydroamination of alkynes compared to the $Au_{36}(SR)_{24}$ cluster with a one-dimensional (1D) arrangement of Au_4 tetrahedral units.[24] Similarly, two isomeric $Au_{38}(PET)_{24}$ (PET = 2-phenylethanethiol) clusters have demonstrated distinctly different catalytic properties, while two isomeric $Au_{42}(TBBT)_{26}$ (TBBT = 4-*tert*-butylbenzenethiol) clusters have exhibited diverse luminescence behaviors.[22,23] Efforts have been made to discover more pairs of nanocluster structural isomers.[25–39] The majority of research on structural isomerism in nanoclusters has focused on gold and silver nanoclusters, with limited exploration of copper nanocluster structural isomerism.[31,40,41] Quasi-structural isomerism has been identified in copper clusters based on the $Cu_{20}H_{11}(S_2P(O^iPr)_2)_9$ and $Cu_{20}H_{11}\{Se_2P(O^iPr)_2\}_9$ templates.[40] Then the Sun group synthesized two quasi-structurally isomeric copper nanoclusters, $[Cu_{13}Na_2(CZ\text{-}PrA)_6(TC_4A)_2Cl(CH_3OH)_2]$ and $[Cu_{13}Na(CZ\text{-}PrA)_6(TC_4A)_2(CH_3OH)]\cdot CH_3OH\cdot CH_2Cl_2\cdot CH_3COCH_3$, with nearly identical Cu_{13} cores but different ligand arrangements. This difference results in varied catalytic selectivity for the $^1O_2$ involved selective oxidation of sulfides.[41] Unlike the quasi-structural isomerism observed in

[a]*Key Laboratory of Structure and Functional Regulation of Hybrid Materials, Anhui University, Ministry of Education, Institutes of Physical Science and Information Technology, Anhui University, Department of Chemistry and Center for Atomic Engineering of Advanced Materials, Anhui University, Hefei, Anhui 230601, P. R. China. E-mail: zmz@ahu.edu.cn, jinshan@ahu.edu.cn*

[b]*School of Food and Chemical Engineering, Shaoyang University, Shaoyang 422000, PR China. E-mail: xionglin0823@gmail.com*

†Electronic supplementary information (ESI) available: Synthesis process, characterization, X-ray analysis, and Fig. S1, S12 and Tables S1–S6 offering more details on the nanoclusters **Cu_{22}-1** and **Cu_{22}-2**. CCDC 2289673 for **Cu_{22}-1** and 2289674 for **Cu_{22}-2**. For ESI and crystallographic data in CIF or other electronic format see DOI: https://doi.org/10.1039/d4nr00973h

‡These authors contributed equally.

copper nanoclusters, reports of copper cluster isomers sharing the same molecular formula yet exhibiting different structures are exceedingly rare. Therefore, further investigations are necessary to explore the isomerism of copper nanoclusters.

In this study, we present the synthesis of two isomeric copper nanoclusters, namely **Cu_{22}-1** and **Cu_{22}-2**, through the reduction of a copper salt ($Cu(CH_3CN)_4{\cdot}BF_4$) in the presence of PhSeH and P(Ph-^{4}F)$_3$ ligands. The compositions of **Cu_{22}-1** and **Cu_{22}-2** were determined to be $Cu_{22}(SePh)_{10}(Se)_6(P(Ph\text{-}^4F)_3)_8$. The Se^{2-} in the clusters may be generated *in situ* by the decomposition of the $PhSe^-$ ligands, whose C–Se bonds are broken under the reducing atmosphere.[42,43] Interestingly, during the crystal culture process, **Cu_{22}-1** and **Cu_{22}-2** formed crystals with different crystal forms (Fig. S1†), enabling easy separation and subsequent analysis using single-crystal X-ray diffraction. Although **Cu_{22}-1** and **Cu_{22}-2** exhibit slight structural differences, they display distinct packing modes and demonstrate unique catalytic properties. This discovery of copper isomerism protected by $PhSe^-$ and P(Ph-^{4}F)$_3$ ligands contributes to the advancement of structural isomerism in this field.

Results and discussion

The synthesis of the two isomeric $Cu_{22}(SePh)_{10}(Se)_6(P(Ph\text{-}^4F)_3)_8$ clusters was achieved using a one-pot method, followed by a crystal culture process to separate them (Scheme 1). In this procedure, $Cu(CH_3CN)_4{\cdot}BF_4$ was added to a mixed solution of CH_3CN and $CHCl_3$. After 10 minutes, tris(4-fluorophenyl)phosphine (P(Ph-^{4}F)$_3$) and phenylselenol (PhSeH) were introduced. After an additional 15 minutes, a $NaBH_4$ solution was added. The resulting mixture was stirred for 4 hours, and then the solution was removed using a rotary evaporator. The obtained precipitate was washed multiple times with CH_2Cl_2 and *n*-hexane. The $Cu_{22}(SePh)_{10}(Se)_6(P(Ph\text{-}^4F)_3)_8$ isomers were crystallized in a mixture of CH_2Cl_2 and *n*-hexane at room temperature for 2 weeks. Black block and yellow flake crystals were observed, which were identified as **Cu_{22}-1** and **Cu_{22}-2**, respectively. The yield of the nanoclusters was about 10% and 15% for black block **Cu_{22}-1** and yellow flake **Cu_{22}-2**, respectively.

Single-crystal structural analysis revealed both copper nanoclusters have identical compositions. Each consisted of 22 copper atoms, 10 $PhSe^-$ ligands, 8 P(Ph-^{4}F)$_3$ and 6 Se atoms, but they had different surface structures. The total structures of **Cu_{22}-1** and **Cu_{22}-2** are shown in Fig. 1. The overall structures of **Cu_{22}-1** and **Cu_{22}-2** are very similar, and the structural isomerism of **Cu_{22}-1** and **Cu_{22}-2** mainly resulted from different arrangements of a few $Cu(SeR)(PR_3)$ motifs which was highlighted by the red and green circles. It is worth noting that the structure of **Cu_{22}-1** was similar to the structures of $[Cu_{22}Se_6(SePh)_{10}(PPh_2C_6H_4SMe)_8]$[44] and $[Cu_{22}Se_6(S\text{-}C_6H_4\text{-}Br)_{10}(PPh_3)_8]/[Cu_{22}Se_6(S\text{-}C_6H_4\text{-}OSiMe_3)_{10}(PPh_3)_8]$ reported by the Fuhr group,[45,46] while **Cu_{22}-2** had not been observed.

The structures of **Cu_{22}-1** and **Cu_{22}-2** were analysed and are presented in Fig. 2. Both clusters had similar $Cu_{16}Se_6$ units, which were formed by the fusion of two distorted Ino decahedra $Cu_{10}Se_3$ through the sharing of four Cu atoms (Fig. S2† and Fig. 2A and B). As shown in Fig. S3,† the arrangement of the $Cu_{16}Se_6$ units in **Cu_{22}-2** was more orderly than that in **Cu_{22}-1**. The $Cu_{16}Se_6$ framework was then surrounded by two $Cu(SeR)_3(PR_3)$ motifs. The isomeric structures of **Cu_{22}-1** and **Cu_{22}-2** were achieved when the surface $Cu_2(SeR)_2(PR_3)_2$ motifs capped the $Cu_{16}Se_6@Cu_2(SeR)_6(PR_3)_2$ framework. As shown in Fig. 2C and D, the difference in the bonding environment of the $Cu_2(SeR)_2(PR_3)_2$ motifs with the $Cu_{16}Se_6@Cu_2(SeR)_6(PR_3)_2$ framework can be observed, especially for the copper atoms (blue). The copper atoms in blue shift from the position near $Cu(SeR)_3(PR_3)$ to the position of the nucleus, accompanied by the bond distance of Cu_{blue}–Se_{red} varying from 2.587 Å to 4.604 Å, and the bond distance of Cu_{blue}–Se_{yellow} varying from 4.446 Å to 2.553 Å (Fig. S4†). Therefore, the different arrangements of the surface motifs account for the isomerism of **Cu_{22}-**

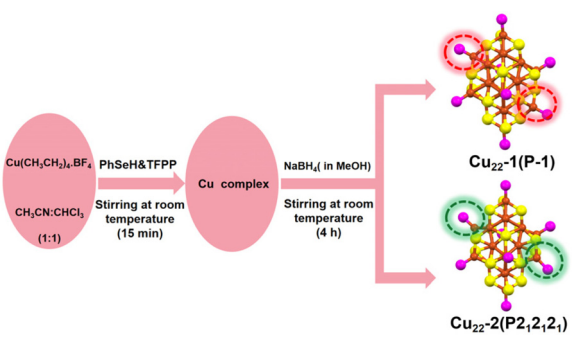

Scheme 1 The synthesis method of **Cu_{22}-1** and **Cu_{22}-2**.

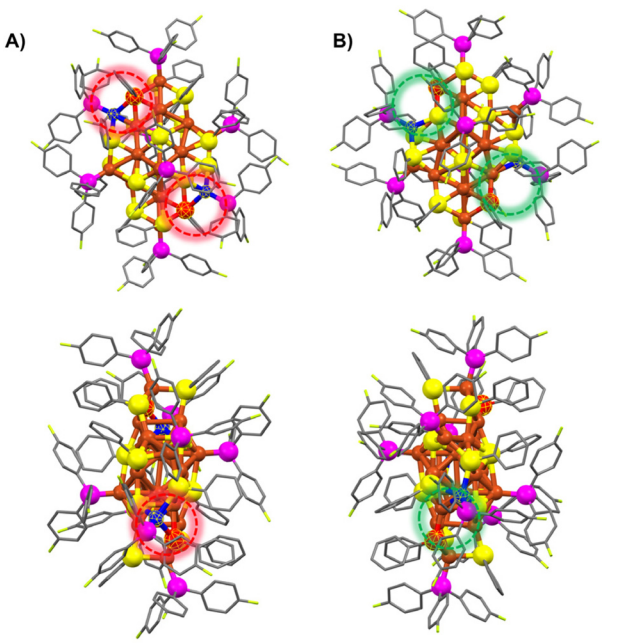

Fig. 1 The total structures of (A) **Cu_{22}-1** and (B) **Cu_{22}-2** from different views. Color labels: Cu = brown/blue, Se = yellow/red, P = purple, F = chartreuse, C = gray. For clarity, H atoms are omitted.

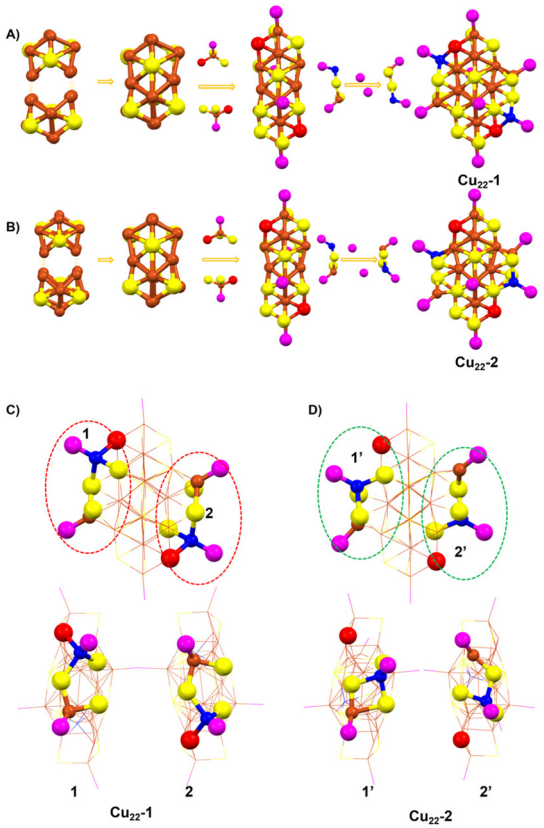

Fig. 2 (A and B) Anatomy of the two Cu_{22} clusters. The copper atoms highlighted in blue and Se atom highlighted in red represent a slight change in bonding patterns in the surface structure. (C and D) The different bonding environments of $Cu_2(SeR)_2(PR_3)_2$ motifs with the $Cu_{16}Se_6@Cu_2(SeR)_6(PR_3)_2$ framework. Cu = brown/blue, Se = yellow/red, P = purple. For clarity, C, H and F atoms are omitted.

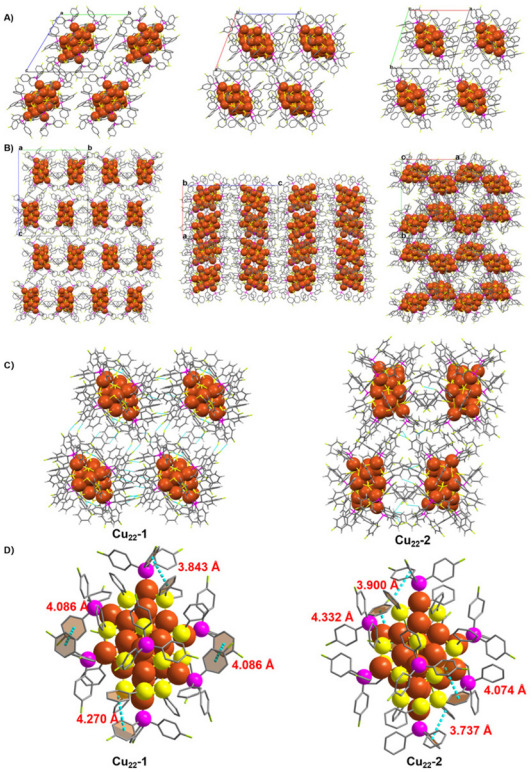

Fig. 3 Views of the assembled packing of (A) **Cu_{22}-1** and (B) **Cu_{22}-2** viewed along the *a*, *b* and *c* axes. (C) The intermolecular forces of C–F···H–C in the isomeric **Cu_{22}-1** and **Cu_{22}-2**. (D) The intramolecular forces of π···π in the isomeric **Cu_{22}-1** and **Cu_{22}-2**. Cu = brown, Se = yellow P = purple, F = chartreuse, C = gray. For clarity, H atoms are omitted.

1 and **Cu_{22}-2** clusters, which is similar to the case of $Au_{23}(C{\equiv}CBu^t)_{15}$ and different from the case of $Au_{38}(PET)_{24}$, where completely different metal cores were observed in the two isomers. The Cu–Cu distances gave an average of 2.647 Å for **Cu_{22}-1** and 2.672 Å for **Cu_{22}-2**, while the Cu–Se distances gave an average of 2.530 Å for **Cu_{22}-1** and 2.519 Å for **Cu_{22}-2**, and the Cu–P distances gave an average of 2.223 Å for **Cu_{22}-1** and 2.228 Å for **Cu_{22}-2** (Fig. S5 and 6†). Furthermore, the differences in bonding modes between the two surface Cu–P ligands and the overall framework were found to be the main cause of isomerism of the **Cu_{22}-1** and **Cu_{22}-2** clusters, as illustrated in Fig. S7.†

Regarding the crystal system, the two isomeric **Cu_{22}-1** and **Cu_{22}-2** clusters exhibit different space groups despite sharing the same crystal condition (CH_2Cl_2 and *n*-hexane). **Cu_{22}-1** crystallized in the triclinic $P\bar{1}$ space group, while **Cu_{22}-2** crystallized in the orthorhombic $P2_12_12_1$ space group (Tables S1 and S2†). In the crystal unit cell of **Cu_{22}-1** (Fig. 3A), only one nanocluster is observed, and these nanoclusters are arranged in the same direction in the packing model. On the other hand, **Cu_{22}-2** nanoclusters in the crystal unit cell are arranged in an alternating pattern (Fig. 3B, and Fig. S8†). This indicates that structural isomerism can effectively alter the stacking pattern of clusters. In the stacking pattern of **Cu_{22}-1** and **Cu_{22}-2**, intermolecular forces such as C–F···H–C interactions are observed (Fig. 3C), with a higher occurrence in the stacking pattern of **Cu_{22}-1**. Furthermore, it is noteworthy that intramolecular π···π interactions have been identified within both isomeric forms of **Cu_{22}-1** and **Cu_{22}-2** (Fig. 3D). These interactions, crucial for the stabilization of molecular structures, exhibit variations that can be attributed to the differing arrangements of surface ligands across the isomers. This observation underscores the significant role that ligand positioning plays in influencing the molecular interactions and, consequently, the overall behavior of these nanoclusters. These intramolecular and intermolecular forces contribute to the efficient stability of the two isomeric **Cu_{22}-1** and **Cu_{22}-2** clusters.

As determined by single-crystal X-ray diffraction (SCXRD), the two isomeric **Cu_{22}-1** and **Cu_{22}-2** clusters were found to have the formula $Cu_{22}(SePh)_{10}(Se)_6(P(Ph\text{-}^4F)_3)_8$, with a total of 22 copper atoms, 10 $SePh^-$ ligands, 6 Se ligands, and 8 $P(Ph\text{-}^4F)_3$ ligands. Both isomeric nanoclusters were found to possess 0 free electrons, calculated as 22 (Cu) − 10 (SePh) − 6 (Se) × 2 − 0 (charge) = 0 e. To further validate the neutral state of the cluster, as indicated by X-ray single-crystal analysis, electrospray ionization time-of-flight mass spectrometry was con-

ducted in both positive and negative modes. No mass signal for the cluster was detected in either the positive or negative ion mode. The solubility of the Cu_{22} clusters was tested in solvents such as toluene, CH_2Cl_2, $CHCl_3$, CH_3OH, CH_3CH_2OH and CH_3CN. Cu_{22} was found to be practically insoluble in CH_3OH, CH_3CH_2OH and CH_3CN, while showing limited solubility in toluene, CH_2Cl_2 and $CHCl_3$. As Cu_{22} exhibits stability for several hours in CH_2Cl_2 solution, CH_2Cl_2 was selected as the solvent for the UV-vis spectral analysis. The UV-vis spectra of **Cu_{22}-1** and **Cu_{22}-2** in CH_2Cl_2 are shown in Fig. 4A and B, respectively. **Cu_{22}-1** exhibited a shoulder band at 420 nm, with the optical energy gap being 2.60 eV, while **Cu_{22}-2** showed a very weak shoulder band at 382 nm, with the optical energy gap being 2.73 eV (Fig. S9†). These distinct UV-vis spectra indicated that the two isomeric **Cu_{22}-1** and **Cu_{22}-2** clusters possess different electronic structures, which could potentially impact their catalytic performance. X-ray photoelectron spectroscopy (XPS) was performed to confirm the formula. XPS analysis demonstrated the Cu/Se/P atomic ratio of 22/11.8/8.3 and 22/12.3/8.2 for **Cu_{22}-1** and **Cu_{22}-2**, respectively, close to the ratio of 22/12/8 obtained from the crystal analysis results. The peak signals of Cu, Se, and P are shown in Fig. 4C and D. This result illustrated that the valence state of Cu in the Cu_{22} nanocluster was close to +1 (Fig. S10†). Elemental analysis (EA) measurement (Table S3†) was performed and the ratio of elements agrees well with that from the X-ray crystallographic analysis. In addition, powder X-ray diffraction (PXRD) was used to assess the purity of the nanoclusters (Fig. 4E and F). The results show that the experimental data is in good agreement with theoretical data, which confirmed their high phase purity. Fluorescence spectroscopy was conducted on the two isomers **Cu_{22}-1** and **Cu_{22}-2** at low temperatures. As illustrated in Fig. S11,† it was observed that both isomers exhibited no fluorescence, whether in solution or in the solid state. Consequently, these findings categorized the two isomers of **Cu_{22}-1** and **Cu_{22}-2** as non-fluorescent clusters.

Furthermore, the electronic structures of isomeric **Cu_{22}-1** and **Cu_{22}-2** were predicted by DFT calculation.[47–51] As depicted in Fig. 5, comparing the partial density-of-states (PDOS) diagrams of **Cu_{22}-1** and **Cu_{22}-2** provides a clearer insight into the atomic distribution within these two cluster structures and their respective contributions to orbitals across different energy levels. This comparative analysis helps to uncover both similarities and distinctions in the electronic structure of the two clusters. From Fig. 5, it is evident that in the low-energy occupied orbital regions of both clusters, the pink and orange curves are relatively prominent, indicating a significant role played by the Cu and Se atoms' orbitals in forming these occupied orbitals in **Cu_{22}-1** and **Cu_{22}-2**. Conversely, the unoccupied orbitals in the higher energy range of the clusters were predominantly composed of C atom orbitals (as shown by the red curve in the PDOS). Furthermore, the DOS diagram reveals that the disparity in the HOMO–LUMO energy gaps between **Cu_{22}-1** and **Cu_{22}-2** is minimal (2.86 eV and 2.73 eV, respectively), suggesting a similarity in their electronic structures. The HOMO–LUMO energy gaps agreed with the optical energy gap

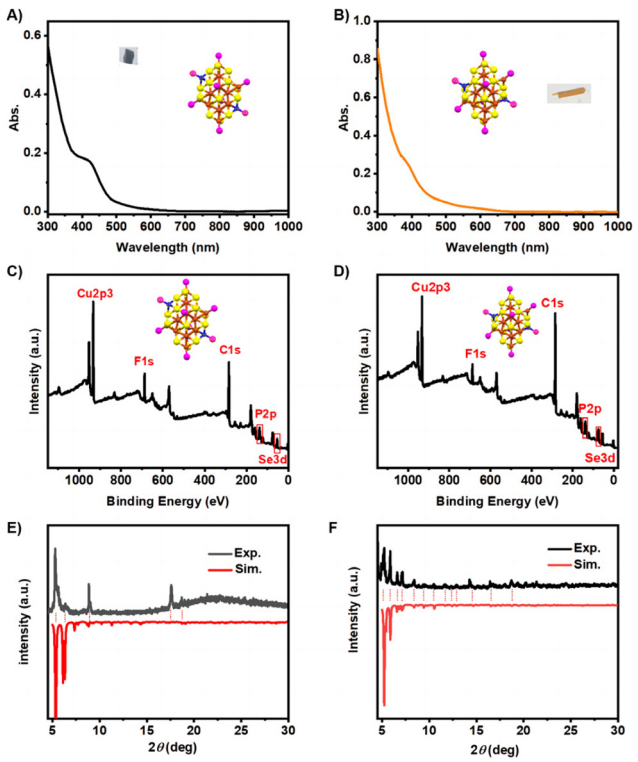

Fig. 4 The UV-vis spectra of isomeric (A) **Cu_{22}-1** dissolved in CH_2Cl_2 and (B) **Cu_{22}-2** slightly dissolved in CH_2Cl_2; the XPS data of (C) **Cu_{22}-1** and (D) **Cu_{22}-2**; the PXRD data of (E) **Cu_{22}-1** and (F) **Cu_{22}-2**.

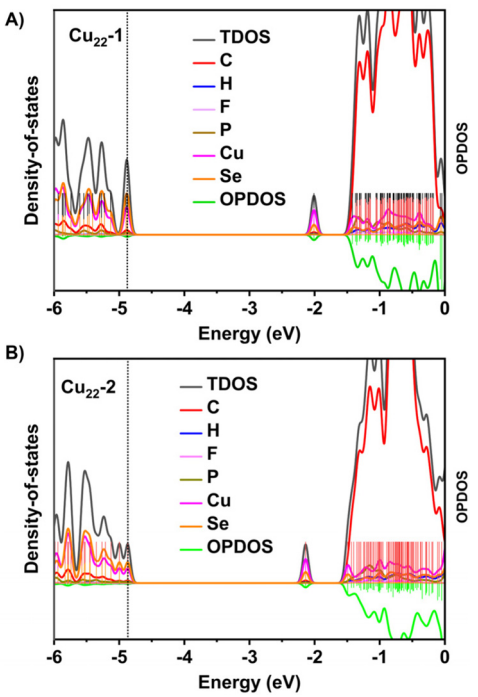

Fig. 5 Calculated PDOS for (A) **Cu_{22}-1** and (B) **Cu_{22}-2**. Here the orbital energy range is set from −6 eV to 0 eV.

well. Nonetheless, there are subtle discrepancies in the DOS curves of the two clusters. Specifically, the TDOS curves (depicted in black) of **Cu_{22}-1** and **Cu_{22}-2** exhibit noticeable distinctions in the vicinity of the −5.0 eV energy level. More precisely, within this energy range, the two orbitals of **Cu_{22}-1** form a distinct higher peak. Conversely, due to a significant energy gap disparity between the two orbitals in **Cu_{22}-2**, under the same broadening function and full width at half maximum (FWHM), the TDOS displays two shorter peaks. This implies that the orbital density in the −5.0 eV to −4.6 eV range differs between the two clusters. Furthermore, with a relative energy difference of 0.39 eV (**Cu_{22}-1** exhibiting lower energy than **Cu_{22}-2**), it is evident that slight variances exist in the electronic structures of **Cu_{22}-1** and **Cu_{22}-2**.

On the other hand, UV-visible absorption spectroscopy (UV-Vis) is a powerful tool to provide structural and electronic structure information, hence the UV-Vis spectra of **Cu_{22}-1** and **Cu_{22}-2** simulated by the TDDFT method provide an effective way to reveal the differences in the structure and electronic structure of the two clusters. Fig. 6A and B show the simulated UV-Vis spectra of **Cu_{22}-1** and **Cu_{22}-2**. It can be seen that the spectral curves of these two clusters have similarities but also show obvious differences. Briefly, both Cu_{22} isomers have four similar absorption peaks, namely peak α, peak β, peak γ and peak δ. For **Cu_{22}-1**, the four absorption peaks of α, β, γ and δ are located at 605 nm, 485 nm, 418 nm and 366 nm, respectively. The corresponding four absorption peaks in **Cu_{22}-2** are located at 623 nm, 499 nm, 402 nm and 367 nm, respectively. Therefore, the electronic structures of the two Cu_{22} are similar to a large extent. The transition modes shown in Tables S4 and 5† reveal the attributions of these absorption peaks. Obviously, the peak α in the two Cu_{22} clusters' spectra has the same attribution, and both are obtained by broadening the first excited state and the second excited state. As shown in Table S4,† for **Cu_{22}-1**, the first excited state is characterized by H → L contributing 66.6%, followed by H−1 → L contributing 31.2%. The second excited state is characterized by an H−1 → L contribution of 66.2%, followed by an H → L contribution of 31.0%. This is very similar to the assignment of the absorption peak α in the **Cu_{22}-2** spectrum (Table S5†). However, Tables S5 and S6† show that there are obvious differences in the assignments of the absorption peaks β, γ and δ in the spectra of the two Cu_{22} clusters. Interestingly, as shown in Fig. 6B, due to the difference in geometric structure, **Cu_{22}-2** has an additional absorption peak θ compared to **Cu_{22}-1** (see Table S6† for its assignment). This shows that there are significant differences in the spectral characteristics of the two Cu_{22} clusters, revealing the differences in their electronic structures. Furthermore, based on the rotatory strength from the ground state to each excited state calculated by TDDFT, we also plotted the electronic circular dichroism (ECD) spectra of the two Cu_{22} clusters, which are shown in Fig. 6C and D. It can be clearly found that the ECD spectra of the two Cu_{22} clusters are significantly different. The reason is that the ECD is extremely sensitive to conformation. Therefore, even if **Cu_{22}-1** and **Cu_{22}-2** only have a small difference in the shell structure, the difference can still be clearly reflected in the ECD.

The variations in surface shell ordering cause structural isomerism, altering the electronic structure, which then will influence the catalytic activity. To explore this, the copper-catalyzed [3 + 2] azide–alkyne cycloaddition (CuAAC) reaction was used as an example reaction, and the activity of **Cu_{22}-1** and **Cu_{22}-2** was evaluated (Table 1 and Table S6†). The reaction was conducted in acetonitrile, using 0.06 mol% of **Cu_{22}-1** and **Cu_{22}-2** crystals as catalysts suspended in the solvent.[52–56] After 24 hours at 50 °C, **Cu_{22}-1** achieved a product yield of 92%, while **Cu_{22}-2** yielded only 36% (Table S6†). A time-dependent kinetic study of the CuAAC reaction was also performed. **Cu_{22}-1** exhibited a catalytic efficiency of 64% at approximately 12 hours, whereas **Cu_{22}-2** had a catalytic efficiency of 32%. With an extended reaction time, **Cu_{22}-1** achieved a catalytic efficiency of 80% at approximately 18 hours and 92% at

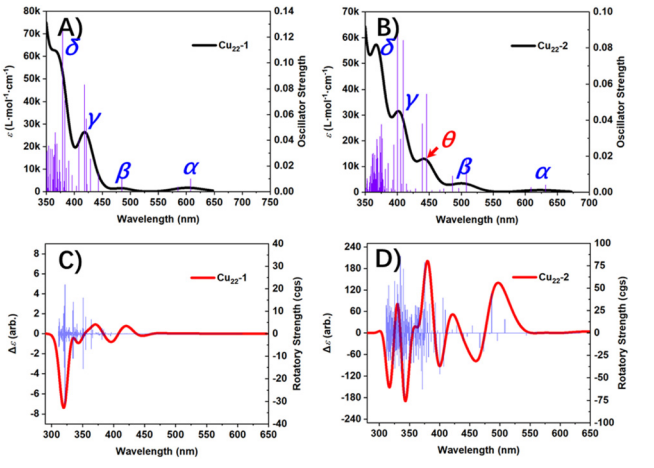

Fig. 6 Simulated UV-visible (UV-Vis) spectra and electronic circular dichroism (ECD) spectra for **Cu_{22}-1** and **Cu_{22}-2** based on the TDDFT method. (A and B) UV-Vis spectra of **Cu_{22}-1** and **Cu_{22}-2**, respectively; (C and D) ECD spectra of **Cu_{22}-1** and **Cu_{22}-2**, respectively.

Table 1 The catalytic performance of isomeric **Cu_{22}-1** and **Cu_{22}-2**. [3 + 2] cycloaddition between benzyl azide and phenylacetylene using isomeric **Cu_{22}-1** and **Cu_{22}-2** as catalysts under visible light[a]

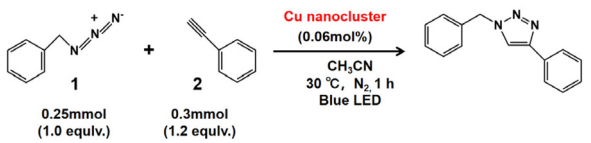

	The product yield determined by GC-MS (%)	
Catalyst[b]	Cycle 1	Cycle 2
Cu_{22}-1	90	89
Cu_{22}-2	10	8

[a] Benzyl azide (0.25 mmol, 1.0 equiv.), phenylacetylene (0.3 mmol, 1.2 equiv.) and acetonitrile (2 mL). [b] With respect to the amount of benzyl azide.

approximately 24 hours (Table S6†). On the other hand, **Cu_{22}-2** reached a catalytic efficiency of 35% at around 18 hours and 36% at around 24 hours. Additionally, due to the absorption peaks near 400 nm in both isomers, a photoinduced catalytic reaction was attempted using 405 nm blue LED irradiation. As shown in Table 1, **Cu_{22}-1** achieved a product yield of 90% after only 1.0 hour of irradiation, while **Cu_{22}-2** yielded only 10%. These differences in catalytic efficiency between **Cu_{22}-1** and **Cu_{22}-2** highlight how the structural isomerism, caused by the arrangement of the outer ligands, can effectively regulate the clusters' catalytic performance. TDDFT calculations indicated that the oscillator strength between the first excited state and the ground state of **Cu_{22}-1** is 0.01004, while in **Cu_{22}-2**, this oscillator strength is only 0.00405, as evidenced by the height of the vertical line representing the lowest excited state in the spectral graph. Typically, an oscillator strength below 0.01 suggests a transition is forbidden, leading us to consider the lowest excited state of **Cu_{22}-2** as a dark state. Therefore, even though the lowest excitation energy of **Cu_{22}-1** is slightly higher than that of **Cu_{22}-2**, the significant oscillator strength of **Cu_{22}-1** facilitates the easy absorption of light at the corresponding frequency to form electron–hole pairs. This attribute makes **Cu_{22}-1** exhibit markedly better photocatalytic activity compared to **Cu_{22}-2**. And as depicted in Fig. S12,† the UV-vis and P-XRD spectra demonstrate significant consistency before and after the photoinduced catalytic reaction, indicating the clusters maintain their integrity during the reaction process.

Conclusions

In summary, we have successfully synthesized and characterized two isomeric copper nanoclusters, $Cu_{22}(SePh)_{10}(Se)_6(P(Ph\text{-}4F)_3)_8$-1 (**$Cu_{22}$-1**, $P\bar{1}$) and $Cu_{22}(SePh)_{10}(Se)_6(P(Ph\text{-}^4F)_3)_8$-2 (**$Cu_{22}$-2**, $P2_12_12_1$), using SCXC. $Cu_{22}(SePh)_{10}(Se)_6(P(Ph\text{-}^4F)_3)_8$ contains a $Cu_{16}Se_6$ core formed by the fusion of two distorted Ino decahedron $Cu_{10}Se_3$ clusters through the sharing of four Cu atoms. This $Cu_{16}Se_6$ core is further capped by two $Cu(SeR)_3(PR_3)$ motifs, two $Cu(SeR)_2(PR_3)_2$ motifs and two PR_3 phosphine ligands. The isomerism of **Cu_{22}-1** and **Cu_{22}-2** is due to the different arrangements of the surface motifs, which result in differences in electronic structure (as manifested by different UV absorption spectra, and DFT calculation) and catalytic efficiency in the copper-catalyzed [3 + 2] azide–alkyne cycloaddition (CuAAC). The clusters are highly stable due to π···π intramolecular interactions and C–F···H–C intermolecular forces, making them difficult to dissolve. These two isomeric copper nanoclusters enrich the development of structural isomerism in copper nanoclusters and provide an opportunity to investigate the structure–function relationship.

Conflicts of interest

There are no conflicts to declare.

Acknowledgements

S. J., Y. Y., M. Z. acknowledge financial support provided by the National Natural Science Foundation of China (21901001, 21631001, 22305002), Anhui Provincial Natural Science Foundation (no. 1908085QB54) and the Scientific Research Program of Anhui Province (2022AH040018). L. X. acknowledges the financial support provided by the National Natural Science Foundation of China (22203053) and the Hunan Provincial Natural Science Foundation (2023JJ40606).

References

1 X. Wang, B. Yin, L. Jiang, C. Yang, G. Zou, S. Chen and M. Zhu, *Science*, 2023, **381**, 784–790.
2 W. Gao, Q. Li, W. Zhong, X. Zhou, Y. Ge, Q. Yan and L. Shang, *Chem. Eng. J.*, 2023, **456**, 140982.
3 X. Ma, J. Li, P. Luo, J. Hu, Z. Han, X. Dong, G. Xie and S. Zang, *Nat. Commun.*, 2023, **14**, 4121.
4 X. Hu, H. Cao, W. Dong and J. Tang, *Talanta*, 2021, **233**, 122480.
5 M. Wang, J. Zhang, X. Zhou, H. Sun and X. Su, *Sens. Actuators, B*, 2022, **358**, 131488.
6 Q. Xue, Z. Wang, S. Han, Y. Liu, X. Dou, Y. Li, H. Zhu and X. Yuan, *J. Mater. Chem. A*, 2022, **10**, 8371–8377.
7 Q. Wu, D. Si, P. Sun, Y. Dong, S. Zheng, Q. Chen, S. Ye, D. Sun, R. Cao and Y. Huang, *Angew. Chem., Int. Ed.*, 2023, **62**, e2023068.
8 S. Zhuang, D. Chen, W. Fan, J. Yuan, L. Liao, Y. Zhao, J. Li, H. Deng, J. Yang, J. Yang and Z. Wu, *Nano Lett.*, 2022, **22**, 7144–7150.
9 L. Liu, Z. Wang, Z. Wang, R. Wang, S. Zang and T. C. W. Mak, *Angew. Chem., Int. Ed.*, 2022, **61**, e2022056.
10 Z. Guan, F. Hu, J. Li, Z. Wen, Y. Lin and Q. Wang, *J. Am. Chem. Soc.*, 2020, **142**, 2995–3001.
11 H. Yi, K. M. Osten, T. I. Levchenko, A. J. Veinot, Y. Aramaki, T. Ooi, M. N. Nambo and C. M. Crudden, *Chem. Sci.*, 2021, **12**, 10436–10440.
12 Y. Chen, C. Liu, Q. Tang, C. Zeng, T. Higaki, A. Das, D. Jiang, N. L. Rosi and R. Jin, *J. Am. Chem. Soc.*, 2016, **138**, 1482–1485.
13 S. Horiuchi, S. Moon, A. Lto, J. Tessarolo, E. S. Y. Arikawa, G. H. Clever and K. Umakoshi, *Angew. Chem., Int. Ed.*, 2021, **60**, 10654–10660.
14 S. Zhuang, L. Liao, M. Li, C. Yao, Y. Zhao, H. Dong, J. Li, H. Deng, L. Lie and Z. Wu, *Nanoscale*, 2017, **9**, 14809–14813.
15 Y. T. Cao, S. Malola, M. F. Matus, T. K. Chen, Q. F. Yao, R. Shi, H. Häkkinen and J. P. Xie, *Chem*, 2021, **7**, 2227–2244.
16 Y. Li, X. Luo, P. Luo, Q. Zang, Z. Wang and S. Zang, *ACS Nano*, 2023, **17**, 5834–5841.
17 S. Knoppe and T. Bürgi, *Acc. Chem. Res.*, 2014, **47**, 1318–1326.

18 W. Yu, D. Hu, L. Xiong, Y. Li, X. Kang, S. Chen, S. Wang, Y. Pei and M. Zhu, *Part. Part. Syst. Charact.*, 2019, **36**, 1800494.
19 S. Yamazoe, S. Matsuo, S. Muramatsu, S. Takano, K. Nitta and T. Tsukuda, *Inorg. Chem.*, 2017, **56**, 8319–8325.
20 N. Xia, J. Yuan, L. Liao, W. Zhang, J. Li, H. Deng, J. Yang and Z. Wu, *J. Am. Chem. Soc.*, 2020, **142**, 12140–12145.
21 X. Liu, W. Xu, X. Huang, E. Wang, X. Cai, Y. Zhao, J. Li, M. Xiao, C. Zhang, Y. Gao, W. Ding and Y. Zhu, *Nat. Commun.*, 2020, **11**, 3349.
22 S. Tian, Y. Li, M. Li, J. Yuan, J. Yang, Z. Wu and R. Jin, *Nat. Commun.*, 2015, **6**, 8667.
23 S. Zhuang, L. Liao, J. Yuan, N. Xia, Y. Zhao, C. Wang, Z. Gan, N. Yan, L. He, J. Li, H. Deng, Z. Guan, J. Yang and Z. Wu, *Angew. Chem., Int. Ed.*, 2019, **58**, 4510–4514.
24 Y. Zhang, A. Tang, X. Cai, J. Xu, G. Li, W. Hu, X. Liu, M. Chen and Y. Zhu, *Nano Res.*, 2023, **16**, 3641–3648.
25 S. Chen, L. Xiong, S. Wang, Z. Ma, S. Jin, H. Sheng, Y. Pei and M. Zhu, *J. Am. Chem. Soc.*, 2016, **138**, 10754–10757.
26 S. Yang, J. Chai, Y. Song, J. Fan, T. Chen, S. Wang, H. Yu, X. Li and M. Zhu, *J. Am. Chem. Soc.*, 2017, **139**, 5668–5671.
27 Y. Song, S. Wang, J. Zhang, X. Kang, S. Chen, P. Li, H. Sheng and M. Zhu, *J. Am. Chem. Soc.*, 2014, **136**, 2963–2965.
28 A. Das, T. Li, G. Li, K. Nobusada, C. Zeng, N. L. Rosi and R. Jin, *Nanoscale*, 2014, **6**, 6458–6462.
29 S. Jin, F. Xu, W. Du, X. Kang, S. Chen, J. Zhang, X. Li, D. Hu, S. Wang and M. Zhu, *Inorg. Chem.*, 2018, **57**, 5114–5119.
30 C. Zeng, T. Li, A. Das, N. L. Rosi and R. Jin, *J. Am. Chem. Soc.*, 2013, **135**, 10011–10013.
31 Y. Bao, X. Wu, B. Yin, X. Kang, Z. Lin, H. Deng, H. Yu, S. Jin, S. Chen and M. Zhu, *Chem. Sci.*, 2022, **13**, 14357–14365.
32 A. Dass, T. Jones, M. Rambukwella, D. Crasto, K. J. Gagnon, L. Sementa, M. D. Vetta, O. Baseggio, E. Aprà, M. Stener and A. Fortunelli, *J. Phys. Chem. C*, 2016, **120**, 6256–6261.
33 T. Higaki, C. Liu, C. Zeng, R. Jin, Y. Chen, N. L. Rosi and R. Jin, *Angew. Chem., Int. Ed.*, 2016, **55**, 6694–6697.
34 R. S. Dhayal, Y. Lin, J.-H. Liao, Y.-J. Chen, Y.-C. Liu, M.-H. Chiang, S. Kahlal, J. Y. Saillard and C. Liu, *Chem. – Eur. J.*, 2016, **22**, 9943–9947.
35 M. W. Heaven, A. Dass, P. S. White, K. M. Holt and R. W. Murray, *J. Am. Chem. Soc.*, 2008, **130**, 3754–3755.
36 M. Zhu, C. M. Aikens, F. J. Hollander, G. C. Schatz and R. Jin, *J. Am. Chem. Soc.*, 2008, **130**, 5883–5885.
37 J. Li, Z. Guan, Z. Lei, F. Hu and Q. Wang, *Angew. Chem., Int. Ed.*, 2019, **58**, 1083–1087.
38 N. Yan, N. Xia, L. Liao, M. Zhu, F. Jin, R. Jin and Z. Wu, *Sci. Adv.*, 2018, **4**, eaat7259.
39 Z. Lei, J. Li, X.-K. Wan, W.-H. Zhang and Q.-M. Wang, *Angew. Chem., Int. Ed.*, 2018, **57**, 8639–8643.
40 R. S. Dhayal, J.-H. Liao, X. Wang, Y.-C. Liu, M.-H. Chiang, S. Kahlal, J.-Y. Saillard and C. W. Liu, *Angew. Chem., Int. Ed.*, 2015, **54**, 13604–13608.
41 C. K. Zhang, Z. Wang, W.-D. Si, L. Y. Wang, J.-M. Dou, Z.-Y. Gao, C.-H. Tung and D. Sun, *ACS Nano*, 2022, **16**, 9598–9607.
42 T. Higaki, C. Liu, M. Zhou, T. Luo, N. L. Rosi and R. Jin, *J. Am. Chem. Soc.*, 2017, **139**, 9994–10001.
43 B. Yan, X. You, X. Tang, J. Sun, Q. Xu, L. Wang, Z.-J. Guan, F. Li and H. Shen, *Chem. Mater.*, 2024, **36**, 1004–1012.
44 O. Fuhr, A. Meredith and D. Fenske, *J. Chem. Soc., Dalton Trans.*, 2002, 4091–4094.
45 R. Langer, L. Wünsche, D. Fenske and O. Fuhr, *Z. Anorg. Allg. Chem.*, 2009, **635**, 2488–2494.
46 R. Langer, W. Yu, L. Wünsche, G. Buth, O. Fuhr and D. Fenske, *Z. Anorg. Allg. Chem.*, 2011, **637**, 1834–1840.
47 H. Li, P. Wang, C. Zhu, W. Zhang, M. Zhou, S. Zhang, C. Zhang, Y. Yun, X. Kang, Y. Pei and M. Zhu, *J. Am. Chem. Soc.*, 2022, **144**, 23205–23213.
48 M. Cui, Y. Shi, X. Ma, Q. Li, L. Chen, L. Zhang, J. Wu, H. Yu and M. Zhu, *ACS Nano*, 2024, **18**, 6591–6599.
49 G. Luo, Z. Pan, B. Han, G. Dong, C. Deng, M. Azam, Y. Tao, J. He, C. Sun and D. Sun, *Angew. Chem., Int. Ed.*, 2023, **62**, e2023068.
50 Z. Wang, Y. Zhu, O. Ahlstedt, K. Konstantinou, J. Akola, C. Tung, F. Alkan and D. Sun, *Angew. Chem., Int. Ed.*, 2024, **63**, e20231451.
51 T. Jia, Z. Guan, C. Zhang, X. Zhu, Y. Chen, Q. Zhang, Y. Yang and D. Sun, *J. Am. Chem. Soc.*, 2023, **145**, 10355–10363.
52 D. Campeau, A. Pommainville, M. Gorodnichy and F. Gagosz, *J. Am. Chem. Soc.*, 2023, **145**, 19018–19029.
53 W. D. G. Brittain, B. R. Buckley and J. S. Fossey, *ACS Catal.*, 2016, **6**, 3629–3636.
54 J. M. Holub and K. Kirshenbaum, *Chem. Soc. Rev.*, 2010, **39**, 1325–1337.
55 C. Dong, R. Huang, A. Sagadevan, P. Yuan, L. G. Arzaluz, A. Ghosh, S. Nematulloev, B. Alamer, O. M. Mohammed, I. Hussain, M. Rueping and O. M. Bakr, *Angew. Chem., Int. Ed.*, 2023, **62**, e20230714.
56 Y. Fang, K. Bao, P. Zhang, H. Sheng, Y. Yun, S. Hu, D. Astruc and M. Zhu, *J. Am. Chem. Soc.*, 2021, **143**, 1768–1772.